Kinetics of thermally induced swelling of hydrogels

Huidi Ji [a], Hashem Mourad [a], Eliot Fried [b], John Dolbow [a,*]

[a] *Department of Civil and Environmental Engineering, Duke University, Durham, NC 27708-0287, USA*
[b] *Department of Mechanical and Aerospace Engineering, Washington University in St. Louis, St. Louis, MO 63130-4899, USA*

Abstract

We present a continuum model for thermally induced volume transitions in stimulus–responsive hydrogels (SRHs). The framework views the transition as proceeding via the motion of a sharp interface separating swollen and collapsed phases of the underlying polymer network. In addition to bulk and interfacial force and energy balances, our model imposes an interfacial normal configurational force balance. To account for the large volume changes exhibited by SRHs during actuation, the governing equations are developed in the setting of finite-strain kinematics. The numerical approximations to the coupled thermomechanical equations are obtained with an extended finite element/level-set method. The solution strategy involves a non-standard operator split and a simplified version of the level-set update. A number of representative problems are considered to investigate the model and compare its predictions to experimental observations. In particular, we consider the thermally induced swelling of spherical and cylindrical specimens. The stability of the interface evolution is also examined.
© 2005 Elsevier Ltd. All rights reserved.

1. Introduction

A hydrogel is a cross-linked macromolecular network immersed in a solvent. Stimulus–responsive hydrogels (SRHs) are synthesized to exhibit large reversible volume transitions ($\sim$1000%) in response to changes in external stimuli such as pH, temperature, solvent concentration, light, and magnetic field.

---

* Corresponding author. Tel.: +1 919 660 5202; fax: +1 919 660 5219.
  E-mail address: jdolbow@duke.edu (J. Dolbow).

The actuation time for an SRH specimen scales with the square of characteristic linear dimension of that specimen. At the microscale, actuation times on the order of milliseconds are possible. SRHs have already been used in a wide range of applications from micro-fluidic sensors/actuators, to optical switches, to pumps/carriers of therapeutic drugs in the bloodstream. As applications utilizing SRHs continue to emerge, models that reliably predict their response and provide insight into structure-property-response relationships are needed.

In this paper we focus attention on the swelling kinetics of temperature-responsive hydrogels, such as those based on poly(*N*-isopropylacrylamide) (PNIPA). As the temperature is increased past a lower critical solution temperature (typically around 33 °C), PNIPA gels decrease their volume dramatically as the underlying polymer network transforms from a swollen state to a collapsed state. The process is reversible; decreasing the temperature gives rise to a large volume expansion. This volume transition is also associated with the uptake and expulsion of solvent; in a collapsed state the polymer chains are hydrophobic, while in a swollen state they are hydrophilic.

Most of the models proposed to describe this process invoke the collective diffusion assumption proposed by Tanaka and Fillmore (1979), an assumption in which the motion of the polymer network is counterbalanced by the generation of stress as well as a drag force between the network and the solvent. Recent experimental observations by Olsen et al. (2000), however, display the motion of a sharp front separating swollen and collapsed phases.

Motivated by these observations, Dolbow et al. (2004) developed a sharp-interface theory for chemically induced volumetric transitions in hydrogels. In contrast to mixture theories that are commonly employed to describe SRH kinetics, our theory employs a chemical potential field to describe solute transport and implicitly accounts for the change in solute concentration across the sharp phase interface. A detailed derivation of the theory and the numerical strategy developed to attain approximate solutions to representative boundary value problems was recently presented by Dolbow et al. (in press). In our previous efforts, attention was confined to isothermal circumstances. In the work described here, we consider the coupled effects of thermal transport and force balance in the context of a sharp interface theory for SRH kinetics. We view this as an important step toward a full-field theory incorporating heat and mass transport and their coupling with the stress response in hydrogels.

As in our previous work, the work reported here relies on a sharp-interface theory. In particular, we utilize the theory developed by Gurtin and Struthers (1990) to describe coherent, diffusionless solid-solid phase transitions. Within that theory, the bulk phases are treated as non-linearly thermoelastic and therefore—as is essential for applications of the kind we consider—are capable of sustaining finite strains and rotations. Adopting the approach of Gibbs (1878), Gurtin and Struthers (1990) account for localized interactions between phases by endowing the interface with thermomechanical structure in the form of excess fields. Of essential importance in the theory of Gurtin and Struthers (1990) are the notions of configurational force and configurational force balance.

Roughly speaking, configurational forces are related to the integrity of the body's material structure and expend power in the transfer of material and in the evolution of defects. In dynamical problems, defect structures, such as phase interfaces and dislocation lines, may move relative to the material. In variational treatments of related equilibrium problems, independent kinematical quantities may be independently varied, and each such variation yields a corresponding Euler–Lagrange balance. In dynamics with general forms of dissipation there is no encompassing variational principle, but experience demonstrates the need for an additional balance associated with the kinematics of the defect. An additional balance of this sort is the relation that ensues when one formally sets the variationally derived expression for the driving force on a defect equal to a linear function of the velocity of that defect. Classical examples of driving forces are those on: dislocations (Peach and Koehler, 1950); triple junctions (Herring, 1951); vacancies, interstitial atoms, and inclusions (Eshelby, 1951); interfaces (Eshelby, 1956, 1970); crack tips (Eshelby, 1956; Atkinson and Eshelby, 1968; Rice, 1968).

Guided by variational treatments in which such a balance is a consequence of the assumption of equilibrium, Gurtin and Struthers (1990) (see also, Gurtin, 1995 and Gurtin, 2000) introduce, as primitive objects, configurational forces together with an independent configurational force balance. In the bulk phases, which are free of defects, the configurational force balance yields no information beyond that already contained in the standard Newtonian force balance and, therefore, is redundant. On the interface, however the configurational force balance yields an evolution equation which generalizes the Gibbs–Thomson relation arising in descriptions of alloy solidification (cf., e.g., Mullins and Sekerka, 1963) and supplements the conventional equations expressing standard force balance and energy balance on the interface.

In its general form, the theory of Gurtin and Struthers (1990) allows for material anisotropy of both the bulk and interfacial constitutive response functions. We specialize the theory in accord with the observed isotropy of gel-like substances. In particular, the swollen and collapsed phases of the material are each characterized by properly invariant isotropic response functions determining the free-energy density and the heat flux. For simplicity, we assume that the free-energy density of the interface is constant and, therefore, coincident with the notion of surface tension. Further, while we account for dissipative transition kinetics, we neglect heat conduction on the interface. Our particular constitutive assumptions lead to final evolution equations of the theory in which the coupling between the bulk motion and temperature fields is much more complicated than it is in the evolution equations arising in our work on chemically induced transitions, equations in which the sole coupling between the bulk fields is through the configurational force balance on the interface.

As in our previous work, we develop equivalent variational forms of the evolution equations and boundary/initial conditions. Enriched approximations to the temperature and deformation fields are developed in the context of the eXtended Finite-Element Method (XFEM), and we employ a level-set representation of the interface. The numerical strategy is similar to that described by Dolbow et al. (in press), with a few notable exceptions. In particular, due to the stronger coupling between the bulk temperature and deformation fields, we develop a non-standard operator split to decouple the bulk equations for energy and force balance. We also employ a greatly simplified version of the level-set update.

The X-FEM (Moës et al., 1999; Dolbow, 1999) is a variation on the partition-of-unity framework (Melenk and Babuška, 1996) for building local, non-polynomial ansatz spaces into an approximation to a bulk field. Building upon the early work of Belytschko and Black (1999) on linear elastic fracture mechanics, the method has been advanced and applied toward the modeling of fracture in polycrystalline microstructures (Sukumar et al., 2003), crack nucleation (Bellec and Dolbow, 2003), and incompresssible hyperelastic materials (Dolbow and Devan, 2004). With regard to the simulation of phase transitions, the "enriched" spaces of the X-FEM allow for the representation of sharp interfaces over meshes that need not explicitly "fit" the interface surface without artificially smearing the bulk field across the interface. A further variation on this theme concerns the eXtended-Finite-Element/Level-Set Method (XFE/LSM) (Ji et al., 2002), wherein both the local solution and geometry of arbitrarily evolving features are represented with evolving functions. The coupling of the two methods was first conceived in Sukumar et al. (2001), and several recent advances have improved the robustness of the XFE/LSM. These include new enrichment functions (Moës et al., 2003) for interfaces and techniques to enforce and evaluate interfacial jump conditions (Ji and Dolbow, 2004; Dolbow et al., in press).

The paper is organized as follows. Section 2 provides an overview of our thermomechanical sharp-interface model of SRH kinetics. Variational formulations of the evolution equations are provided in Section 3 together with the numerical strategy of the eXtended Finite-Element/Level-Set Method (XFE/LSM). We then begin our numerical investigations of the theory in Section 4 by considering the response of spherical specimens to thermal actuation. The stability of the phase change is further studied by examining the thermomechanical response of cylindrical specimens with perturbed phase interfaces. Finally, a summary and concluding remarks are given in the last section.

2. Formulation

To account for the roles of deformation and thermal transport in the swelling of hydrogels, we work with the sharp-interface theory of Gurtin and Struthers (1990) specialized to account for the isotropy of gel-like substances.

2.1. Kinematics

We label the swollen and collapsed phases by α and β and write $\mathcal{S}$ for the interface, which we take to divide the region $\mathcal{R}$ occupied by the body into complementary subregions $\mathcal{R}_\alpha(t)$ and $\mathcal{R}_\beta(t)$. We use Grad and Div to denote the gradient and allied divergence operators in the bulk phases, $\text{Div}_\mathcal{S}$ to denote the divergence operator on the interface, and a superposed dot to indicate partial differentiation with respect to time.

We confine our attention to circumstances under which $\mathcal{S}(t)$ is, for each t, a smoothly orientable surface that evolves smoothly in time. We write $\mathbf{n}$ for the unit normal on $\mathcal{S}$, directed outward from $\mathcal{R}_\alpha$ as shown in Fig. 1, v for the (scalar) normal velocity of $\mathcal{S}$ in the direction of $\mathbf{n}$, and $\mathsf{K} = -\text{Div}_\mathcal{S}\mathbf{n}$ is for the total (i.e., twice the mean) interfacial curvature.

Aside from the configuration of $\mathcal{S}$, the primary unknowns of the theory are the deformation $\mathbf{y}$ of the polymer network and the absolute temperature θ. Of basic importance are the assumptions of coherency

$$[\![\mathbf{y}]\!] = \mathbf{0} \tag{2.1}$$

and local thermal equilibrium

$$[\![\theta]\!] = 0, \tag{2.2}$$

where $[\![g]\!] = \overset{+}{g} - \overset{-}{g}$, with $\overset{+}{g}$ the interfacial limit of a bulk field g from within the collapsed phase and $\overset{-}{g}$ the corresponding limit from within the swollen phase.

2.2. Bulk and interfacial equations

With a view to focusing on the processes of interfacial motion and bulk diffusion, we neglect inertia. Further, with the exception of a constant interfacial tension, we neglect the thermomechanical structure of the phase interface. Further, we neglect all external supplies.
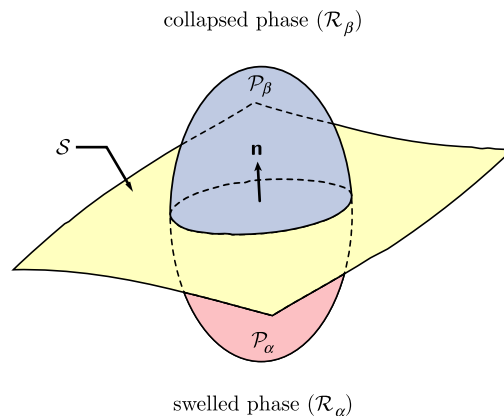

Fig. 1. Schematic indicating: the regions occupied by the swollen and collapsed phases; the evolving interface $\mathcal{S}$, with unit normal $\mathbf{n}$ directed into the collapsed phase; a fixed control volume $\mathcal{P}$ divided by $\mathcal{S}$ into time-dependent regions $\mathcal{P}_\alpha$ and $\mathcal{P}_\beta$ in the swollen and collapsed phases.

In each bulk phase, the basic equations of the theory express deformational force balance, moment balance, and energy balance. Writing $\mathbf{S}_\gamma$, ε_γ, and $\mathbf{q}_\gamma$ for the Piola stress, internal energy density, and heat flux in phase γ, those equations read

$$\left.\begin{aligned}
&\mathrm{Div}\,\mathbf{S}_\gamma = \mathbf{0},\\
&\mathbf{S}_\gamma\mathbf{F}^\top = \mathbf{F}\mathbf{S}_\gamma^\top,\\
&\dot{\varepsilon}_\gamma = \mathbf{S}_\gamma \cdot \dot{\mathbf{F}} - \mathrm{Div}\,\mathbf{q}_\gamma,
\end{aligned}\right\} \tag{2.3}$$

where $\mathbf{F} = \mathrm{Grad}\,\mathbf{y}$ denotes the deformation gradient.

On the interface, the basic equations of the theory express deformational force balance, energy balance, and normal configurational force balance. Of these, the last is a generalization, appropriate to the present context, of the Gibbs–Thomson relation utilized in theories of alloy solidification. Writing η_γ for the entropy density of phase γ, σ for the interfacial tension, and f for the normal component of the internal interfacial configurational force density, these equations read

$$\left.\begin{aligned}
&[\![\mathbf{S}_\gamma]\!]\mathbf{n} = \mathbf{0},\\
&([\![\varepsilon_\gamma - \mathbf{S}_\gamma\mathbf{n}\cdot\mathbf{F}\mathbf{n}]\!] + \sigma\mathsf{K})\mathsf{v} = [\![\mathbf{q}_\gamma]\!]\cdot\mathbf{n},\\
&[\![\varepsilon_\gamma - \theta\eta_\gamma - \mathbf{S}_\gamma\mathbf{n}\cdot\mathbf{F}\mathbf{n}]\!] + \sigma\mathsf{K} + \mathsf{f} = 0.
\end{aligned}\right\} \tag{2.4}$$

These interfacial equations are supplemented by the conditions (2.1) and (2.2) of coherency and local thermal equilibrium. Since we neglect interfacial deformational stress, moment balance is satisfied trivially on the interface.

2.3. Constitutive equations

To close the bulk and interfacial equations (2.3) and (2.4), we provide constitutive equations for the bulk free-energy density ψ_γ and heat flux $\mathbf{q}_\gamma$ of each phase γ and for the internal interfacial configurational force f. Consistent with the isotropy of gel-like substances, we take these equations to be isotropic.

Motivated by the works of Chadwick (1974) and Chadwick and Creasy (1984), we assume that the free-energy density of phase γ is given by

$$\psi_\gamma = \widehat{\psi}_\gamma(\mathbf{F},\theta) = \frac{\theta}{\theta_\gamma}W_\gamma(\imath(\mathbf{B})) + J_\gamma^{\frac{2}{3}}w_\gamma + c\theta\left(1 - \log\frac{\theta}{\theta_\gamma}\right) \tag{2.5}$$

with $\mathbf{B} = \mathbf{F}\mathbf{F}^\top$ the right Cauchy–Green tensor, θ_γ a reference temperature for phase γ, and c the constant specific heat (assumed identical for both phases). Bearing in mind the thermodynamic relations $\varepsilon_\gamma = \psi_\gamma + \theta\eta_\gamma$ and $\eta_\gamma = -\partial\widehat{\psi}_\gamma(\mathbf{F},\theta)/\partial\theta$, the difference

$$\ell = [\![\varepsilon_\gamma]\!] = [\![J_\gamma^{\frac{2}{3}}w_\gamma]\!], \tag{2.6}$$

represents the latent heat of swelling. Without loss of generality, we take

$$J_\beta = 1 \quad \text{and} \quad w_\beta = 0. \tag{2.7}$$

Since α is the swollen phase, we must necessarily have

$$J_\alpha > 1; \tag{2.8}$$

further, it follows from (2.6)–(2.8) that

$$\ell = -J_\alpha^{\frac{2}{3}}w_\alpha. \tag{2.9}$$

To embody experimental observations showing that most gel specimens swell and collapse at sufficiently low and high temperatures, respectively, we assume that

$$\theta_\beta < \theta_\alpha \quad \text{and} \quad w_\alpha < 0. \tag{2.10}$$

These choices lead to the swollen and collapsed phases being energetically preferable (upon neglecting mechanical contributions to ψ_γ) at sufficiently low and high temperatures, respectively. We remark that they also give rise to a positive latent heat of swelling.

For specificity, we assume that W_γ has the form

$$W_\gamma(\imath(\mathbf{B})) = \frac{\mu_\gamma}{2}\left(I_1(\mathbf{B}) - 2J_\gamma^{\frac{2}{3}}\log\left(\frac{\sqrt{I_3(\mathbf{B})}}{J_\gamma}\right) - 3J_\gamma^{\frac{2}{3}}\right) + \frac{\lambda_\gamma J_\gamma^{\frac{2}{3}}}{4}\left(\left(\frac{\sqrt{I_3(\mathbf{B})}}{J_\gamma}\right)^2 + \log^2\left(\frac{\sqrt{I_3(\mathbf{B})}}{J_\gamma}\right)\right) \quad (2.11)$$

with $\mu_\gamma > 0$ and $\lambda_\gamma > 0$ mechanical moduli for phase γ. It can be shown that phase γ is stress-free at the energetically preferred dilatation $\mathbf{F} = J_\gamma\mathbf{I}$, and that μ_γ and λ_γ correspond to conventional shear and Lamé moduli for infinitesimal deviations about this stress-free state (Dolbow et al., 2004).

For the heat flux of phase γ, we assume simply that

$$\mathbf{q}_\gamma = -k_\gamma\mathrm{Grad}\,\theta \quad (2.12)$$

with $k_\gamma > 0$ the constant (scalar) thermal conductivity of phase γ.

In general, the internal configurational force is a drag force that describes the kinetics of the phase transition. For simplicity, we restrict attention to linear transition kinetics, in which case

$$\mathsf{f} = -\frac{\mathsf{v}}{M} \quad (2.13)$$

with $M > 0$ the interfacial mobility.

2.4. Evolution equations

On combining the bulk field equations $(2.3)_1$ and $(2.3)_3$ expressing deformational force balance and energy balance, the constitutive equations (2.5) and (2.12) for the free-energy density and heat flux, and the thermodynamic relations $\mathbf{S}_\gamma = \partial\widehat{\psi}_\gamma(\mathbf{F},\theta)/\partial\mathbf{F}$ and $\eta_\gamma = -\partial\widehat{\psi}_\gamma(\mathbf{F},\theta)/\partial\theta$, we arrive at bulk evolution equations

$$\left.\begin{aligned}
&\mathrm{Div}\left(\frac{\theta}{\theta_\gamma}\frac{\partial W_\gamma(\imath(\mathbf{B}))}{\partial\mathbf{F}}\right) = \mathbf{0}, \\
&c\dot\theta = k_\gamma\mathrm{Div}(\mathrm{Grad}\,\theta) + \frac{\theta}{\theta_\gamma}\frac{\partial W_\gamma(\imath(\mathbf{B}))}{\partial\mathbf{F}}\cdot\dot{\mathbf{F}},
\end{aligned}\right\} \quad (2.14)$$

valid for each phase γ. A direct calculation shows that, together, the constitutive equation (2.5) and the thermodynamic relation $\mathbf{S}_\gamma = \partial\widehat{\psi}_\gamma(\mathbf{F},\theta)/\partial\mathbf{F}$ guarantee satisfaction of the moment balance $(2.3)_2$.

Further, on combining the interfacial field equation $(2.4)_{1,2,3}$ expressing deformational force balance, energy balance, and normal configurational force balance, the constitutive equations (2.5), (2.12), and (2.13) for the free-energy density, heat flux, and interfacial internal configurational force, we arrive at the interfacial evolution equations

$$\left.\begin{aligned}
&\left[\!\left[\frac{\theta}{\theta_\gamma}\frac{\partial W_\gamma(\imath(\mathbf{B}))}{\partial\mathbf{F}}\right]\!\right]\mathbf{n} = \mathbf{0}, \\
&\left(\ell - \left[\!\left[\frac{\theta}{\theta_\gamma}\frac{\partial W_\gamma(\imath(\mathbf{B}))}{\partial\mathbf{F}}\mathbf{n}\cdot\mathbf{F}\mathbf{n}\right]\!\right] + \sigma\mathsf{K}\right)\mathsf{v} + [\![k_\gamma\mathrm{Grad}\,\theta]\!]\cdot\mathbf{n} = 0, \\
&\ell + \mathsf{e} + c[\![\log\theta_\gamma]\!]\theta + \sigma\mathsf{K} = \frac{\mathsf{v}}{M},
\end{aligned}\right\} \quad (2.15)$$

where we have introduced the mechanical driving traction

$$\mathsf{e} = \mathbf{n}\cdot[\![\mathbf{E}_\gamma]\!]\mathbf{n} \quad (2.16)$$

with

$$\mathbf{E}_\gamma = \frac{\theta}{\theta_\gamma} \left(W_\gamma(\imath(\mathbf{B}))\mathbf{I} - \mathbf{F}^\top \frac{\partial W_\gamma(\imath(\mathbf{B}))}{\partial \mathbf{F}} \right) \tag{2.17}$$

representing the essentially mechanical contribution to the Eshelby (or configurational stress) tensor for phase γ.

In contrast to the evolution equations studied by Dolbow et al. (2004), where coupling between the bulk fields is only through the normal configurational force balance, the final governing equations (2.14) and (2.15) of the theory presented here involve a non-trivial coupling between the deformation and the temperature.

2.5. Boundary conditions

Writing $\mathbf{v}$ for the unit orientation of $\partial\mathcal{R}$, directed outward from $\mathcal{R}$, we assume that

$$\mathbf{y}|_{(\partial\mathcal{R})_m} = \bar{\mathbf{y}} \quad \text{and} \quad (\mathbf{S}\mathbf{v})|_{(\partial\mathcal{R})_t} = \mathbf{s} \tag{2.18}$$

with $(\partial\mathcal{R})_m$ and $(\partial\mathcal{R})_t$ complementary subsets of $\partial\mathcal{R}$, and that

$$\theta|_{(\partial\mathcal{R})_p} = \bar{\theta} \quad \text{and} \quad (\mathbf{q} \cdot \mathbf{v})|_{(\partial\mathcal{R})_f} = \bar{q} \tag{2.19}$$

with $(\partial\mathcal{R})_p$ and $(\partial\mathcal{R})_f$ complementary subsets of $\partial\mathcal{R}$.

2.6. Normalized evolution equations

To simplify our analysis, we suppose that L and T denote a characteristic length and time and introduce the dimensionless independent variables

$$\mathbf{x}^* = \frac{\mathbf{x}}{L}, \quad t^* = \frac{t}{T}, \tag{2.20}$$

dependent variables[1]

$$\left. \begin{aligned} \mathbf{y}^*(\mathbf{x}^*, t^*) &= \frac{\mathbf{y}(\mathbf{x}, t)}{L}, \quad \theta^*(\mathbf{x}^*, t^*) = \frac{\theta(\mathbf{x}, t)}{\theta_\alpha}, \\ \mathsf{v}^*(\mathbf{x}^*, t^*) &= \frac{T\mathsf{v}(\mathbf{x}, t)}{L}, \quad \mathsf{K}^*(\mathbf{x}^*, t^*) = L\mathsf{K}(\mathbf{x}, t), \end{aligned} \right\} \tag{2.21}$$

and material parameters

$$\left. \begin{aligned} \mu_\gamma^* &= \frac{\mu_\gamma}{c\theta_\alpha}, \quad \lambda_\gamma^* = \frac{\lambda_\gamma}{c\theta_\alpha}, \quad c^* = c, \quad J_\gamma^* = J_\gamma, \quad k_\gamma^* = \frac{k_\gamma T}{c\theta_\alpha L^2}, \\ \theta_\beta^* &= \frac{\theta_\beta}{\theta_\alpha}, \quad \theta_\alpha^* = 1, \\ \ell^* &= \frac{\ell}{c\theta_\alpha}, \quad \sigma^* = \frac{\sigma}{c\theta_\alpha L}, \quad M^* = \frac{Mc\theta_\alpha T}{L}. \end{aligned} \right\} \tag{2.22}$$

The normalized evolution equations are then

$$\left. \begin{aligned} &\text{Div}\left(\frac{\theta^*}{\theta_\gamma^*} \frac{\partial W_\gamma^*(\imath(\mathbf{B}))}{\partial \mathbf{F}} \right) = \mathbf{0}, \\ &\dot{\theta}^* = k_\gamma^* \text{Div}(\text{Grad}\,\theta^*) + \frac{\theta^*}{\theta_\gamma^*} \frac{\partial W_\gamma^*(\imath(\mathbf{B}))}{\partial \mathbf{F}} \cdot \dot{\mathbf{F}} \end{aligned} \right\} \tag{2.23}$$

---

[1] In (2.21)$_3$ and (2.21)$_4$, it is assumed that $\mathbf{x}$ lies on $\mathcal{S}(t)$.

in each bulk phase γ and

$$
\left.
\begin{aligned}
&\left[\!\!\left[\frac{\theta^*}{\theta_\gamma^*} \frac{\partial W_\gamma^*(\iota(\mathbf{B}))}{\partial \mathbf{F}} \mathbf{n} \right]\!\!\right] = \mathbf{0}, \\
&\left(\ell^* - \left[\!\!\left[\frac{\theta^*}{\theta_\gamma^*} \frac{\partial W_\gamma^*(\iota(\mathbf{B}))}{\partial \mathbf{F}} \mathbf{n} \cdot \mathbf{Fn} \right]\!\!\right] + \sigma^* \mathsf{K}^* \right) \mathsf{v}^* + [\![k_\gamma^* \mathrm{Grad}\, \theta^*]\!] \cdot \mathbf{n} = 0, \\
&\ell^* + \mathsf{e}^* + [\![\log \theta_\gamma^*]\!] \theta^* + \sigma^* \mathsf{K}^* = \frac{\mathsf{v}^*}{M^*}
\end{aligned}
\right\}
\tag{2.24}
$$

on the interface. For convenience, we hereafter omit the superscript asterisks and the explicit mention of both collapsed (α) and swollen (β) phases. Unless otherwise specified, all reported quantities are normalized.

3. Numerical strategy

3.1. Operator split

For the purpose of efficiency, we employ an operator split to solve the coupled system (2.23) and (2.24) of bulk and interfacial evolution equations. In our operator split, the mechanical problem is solved in the first stage with the temperature field held fixed, and then a thermal problem is solved in the second stage. The governing equations at each stage are

Stage I (Mechanical)

$$
\left.
\begin{aligned}
&\mathrm{Div}\left(\frac{\theta}{\theta_\gamma} \frac{\partial W(\iota(\mathbf{B}))}{\partial \mathbf{F}} \right) = \mathbf{0}, \\
&\dot{\theta} = 0.
\end{aligned}
\right\}
\tag{3.1}
$$

Stage II (Thermal)

$$
\left.
\begin{aligned}
&\dot{\mathbf{y}} = \mathbf{0}, \\
&\dot{\theta} = k_\gamma \mathrm{Div}(\mathrm{Grad}\, \theta) + \frac{\theta}{\theta_\gamma} \frac{\partial W_\gamma(\iota(\mathbf{B}))}{\partial \mathbf{F}} \cdot \dot{\mathbf{F}}.
\end{aligned}
\right\}
\tag{3.2}
$$

Although the above strategy does share some common features with so-called "isothermal" splits, there are several important differences that we discuss in the following sections.

3.2. Variational formulation

3.2.1. Weak statement of the deformational force balance and normal interfacial force balance

We let $\mathcal{A}_m$ denote the space of kinematically admissible motions that are sufficiently regular and comply with the Dirichlet boundary condition $(2.18)_1$. Motions in $\mathcal{A}_m$ automatically satisfy the coherency condition (2.1). We let $\mathcal{V}_m$ denote the corresponding space of suitable variations with vanishing values on the essential boundary. Upon multiplying each term of the bulk force balance $(3.1)_1$ by an arbitrary weight function $\mathbf{w}$ in $\mathcal{V}_m$, integrating the resulting equation over $\mathcal{R} \setminus \mathcal{S}$, and integrating by parts, we obtain the variational boundary-value-problem: find $\mathbf{y}$ in $\mathcal{A}_m$ such that

$$\sum_{\gamma=\alpha,\beta} \int_{\mathcal{R}_\gamma} \frac{\theta}{\theta_\gamma} \frac{\partial W_\gamma(\mathbf{F})}{\partial \mathbf{F}} \cdot \mathrm{Grad}\,\mathbf{w}\,\mathrm{d}v = \int_{(\partial\mathcal{R})_t} \mathbf{s} \cdot \mathbf{w}\,\mathrm{d}a \tag{3.3}$$

for all variations $\mathbf{w}$ in $\mathcal{V}_m$. In the derivation of the above, we have used the interfacial force balance (2.24)$_1$.

3.2.2. Weak statement of heat conduction, interfacial energy balance, and interfacial configurational force balance

In the thermal stage, we consider the space $\mathcal{A}_\theta$ of sufficiently regular temperature fields satisfying the Dirichlet boundary condition (2.19)$_1$. We use $\mathcal{V}_\theta$ to denote the space of variations in the temperature. Upon multiplying each term of the bulk heat conduction equation (3.2)$_2$ by an arbitrary variation w in $\mathcal{V}_\theta$, integrating the resulting equation over $\mathcal{R} \setminus \mathcal{S}$, and integrating by parts, we obtain

$$\sum_{\gamma=\alpha,\beta} \int_{\mathcal{R}_\gamma} (\dot{\theta}w + k_\gamma \mathrm{Grad}\,\theta \cdot \mathrm{Grad}\,w)\,\mathrm{d}v + \int_{\mathcal{S}} [\![k_\gamma \mathrm{Grad}\,\theta]\!] \cdot \mathbf{n}w\,\mathrm{d}a$$
$$= \sum_{\gamma=\alpha,\beta} \int_{\mathcal{R}_\gamma} \left(\frac{\theta}{\theta_\gamma} \frac{\partial W_\gamma(\imath(\mathbf{B}))}{\partial \mathbf{F}} \cdot \dot{\mathbf{F}} \right) w\,\mathrm{d}v + \int_{(\partial\mathcal{R})_f} \bar{q}w\,\mathrm{d}a. \tag{3.4}$$

Next, we eliminate the velocity v between the interfacial energy balance (2.24)$_2$ and the interfacial configurational balance (2.24)$_3$ to yield

$$[\![k_\gamma \mathrm{Grad}\,\theta]\!] \cdot \mathbf{n} = \alpha\left(\theta + \frac{\ell + \mathsf{e} + \sigma\mathsf{K}}{[\![\log\theta_\gamma]\!]} \right), \tag{3.5}$$

where we have introduced

$$\alpha = -M(\ell - \mathsf{p} + \sigma\mathsf{K})[\![\log\theta_\gamma]\!] \quad \text{with } \mathsf{p} = [\![\frac{\theta}{\theta_\gamma} \frac{\partial W_\gamma(\imath(\mathbf{B}))}{\partial \mathbf{F}}\mathbf{n} \cdot \mathbf{Fn}]\!]. \tag{3.6}$$

Finally, substituting (3.5) into (3.4) and rearranging terms, we obtain the variational boundary-value problem: find θ in $\mathcal{A}_\theta$ such that

$$\sum_{\gamma=\alpha,\beta} \int_{\mathcal{R}_\gamma} (\dot{\theta}w + k_\gamma \mathrm{Grad}\,\theta \cdot \mathrm{Grad}\,w)\,\mathrm{d}v + \int_{\mathcal{S}} \alpha\theta w\,\mathrm{d}a = \sum_{\gamma=\alpha,\beta} \int_{\mathcal{R}_\gamma} sw\,\mathrm{d}v + \int_{(\partial\mathcal{R})_f} \bar{q}w\,\mathrm{d}a + \int_{\mathcal{S}} \alpha\theta_g w\,\mathrm{d}a \tag{3.7}$$

for all variations w in $\mathcal{V}_\theta$, where

$$\theta_g = -\frac{\ell + \mathsf{e} + \sigma\mathsf{K}}{[\![\log\theta_\gamma]\!]} \quad \text{and} \quad s = \frac{\theta}{\theta_\gamma} \frac{\partial W_\gamma(\imath(\mathbf{B}))}{\partial \mathbf{F}} \cdot \dot{\mathbf{F}}. \tag{3.8}$$

Eq. (3.7) is equivalent to imposing the bulk energy balance (2.23)$_2$, the boundary conditions (2.19) and (3.5).

3.3. Representation of the interface

We represent the interface as the zero-level set

$$\mathcal{S}(t) = \{\mathbf{x} : \zeta(\mathbf{x}, t) = 0\} \tag{3.9}$$

of a function ζ and, following Osher and Sethian (1988), insist that ζ satisfy

$$\dot{\zeta} + v^e|\mathrm{Grad}\,\zeta| = 0 \tag{3.10}$$

with the extension velocity v^e constructed to obey

$$v^e|_{\zeta=0} = \mathsf{v} = -\frac{[\![k_\gamma \mathrm{Grad}\,\theta]\!] \cdot \mathbf{n}}{\ell - \mathsf{p} + \sigma\mathsf{K}}, \tag{3.11}$$

where we have used $(2.24)_2$. We take $\zeta > 0$ in the collapsed phase and $\zeta < 0$ in the swollen phase. The normal $\mathbf{n}$ and total curvature K of the interface can be expressed in terms of the function ζ via

$$\mathbf{n} = \frac{\mathrm{Grad}\,\zeta}{|\mathrm{Grad}\,\zeta|} \quad \text{and} \quad \mathsf{K} = -\mathrm{Div}\left(\frac{\mathrm{Grad}\,\zeta}{|\mathrm{Grad}\,\zeta|}\right). \tag{3.12}$$

Our variational form for the level-set equation (3.10) is based on the assumption that the field ζ is approximately a signed-distance function to the interface, and thus satisfies $|\mathrm{Grad}\,\zeta| = 1$. Accordingly, we follow Mourad and Garikipati (in press) and first replace (3.10) by

$$\dot\zeta + v^e = 0. \tag{3.13}$$

Writing $\mathcal{A}_\zeta$ for the space of admissible level-set fields, the variational equivalent to (3.13) is given by: find $\zeta \in \mathcal{A}_\zeta$ such that

$$\int_{\mathcal{R}} \dot\zeta w \, \mathrm{d}v = -\int_{\mathcal{R}} v^e w \, \mathrm{d}v \tag{3.14}$$

for all $w \in \mathcal{A}_\zeta$. Eq. (3.14) is equivalent to enforcing the interfacial energy balance $(2.24)_2$. Together with (3.7), the normal configurational force balance $(2.24)_3$ is also imposed.

3.3.1. Domain integral approximations to interfacial quantities

In Dolbow et al. (in press), we demonstrated the advantage of approximating interfacial quantities such as the mechanical driving traction e, the curvature K, and normal $\mathbf{n}$ with integral-based expressions that are more amenable for evaluation with weighted-residual methods. Here, we provide only the main results.

Consider an arbitrary point $\mathbf{x}_d$ on the interface where some interfacial quantity is desired. Let w_d denote a sufficiently smooth scalar-valued weight function with compact support $\mathcal{B} = \mathrm{supp}(w_d)$ disjoint from $(\partial\mathcal{R})_n$, so that $\mathcal{B} \cap (\partial\mathcal{R})_n = \emptyset$, and containing $\mathbf{x}_d$. We use $\mathcal{B}_\alpha$ and $\mathcal{B}_\beta$ to denote the bulk domains formed by intersections of $\mathcal{B}$ with $\mathcal{R}_\alpha$, respectively, and $\mathcal{R}_\beta$ and $\mathcal{L} = \mathcal{B} \cap \mathcal{S}$ to denote the portion of the interface that lies within $\mathcal{B}$ (Fig. 2).
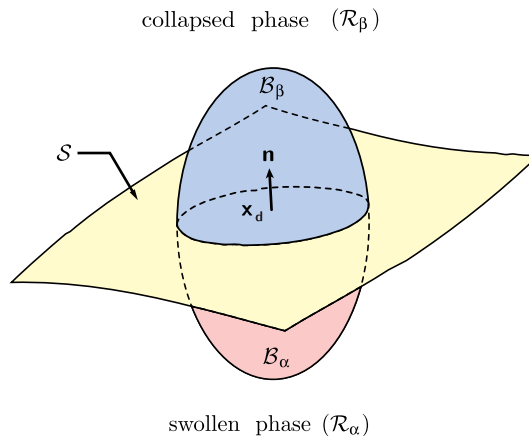

Fig. 2. Local domain $\mathcal{B}$ corresponding to the support of a weight function w_d partitioned into complementary subsets $\mathcal{B}_\alpha$ and $\mathcal{B}_\beta$ in the vicinity of point x_d on the interface $\mathcal{S}$.

Assuming that e is constant over $\mathcal{L}$, it can be shown that

$$e(\mathbf{x}_d) \approx -\frac{\sum_{\gamma=\alpha,\beta} \int_{\mathcal{B}_\gamma} \mathbf{n}^e \cdot \mathbf{E}_\gamma(\theta, \mathbf{F}) \operatorname{Grad} w_d \, \mathrm{d}v}{\int_{\mathcal{L}} w_d \, \mathrm{d}a}, \tag{3.15}$$

where $\mathbf{n}^e$ denotes the extension of the interface normal to points not on the interface, obtained via the function ζ through $(3.12)_1$.

Next, we consider the jump

$$j = [\![k_\gamma \operatorname{Grad} \theta]\!] \cdot \mathbf{n}, \tag{3.16}$$

of the normal component of heat flux across the interface. Again, assuming that j is constant over $\mathcal{L}$, it can be shown that

$$j(\mathbf{x}_d) \approx -\frac{\sum_{\gamma=\alpha,\beta} \int_{\mathcal{B}_\gamma} (\dot{\theta} w_d - s w_d + k_\gamma \operatorname{Grad} \theta \cdot \operatorname{Grad} w_d) \, \mathrm{d}v}{\int_{\mathcal{L}} w_d \, \mathrm{d}a}. \tag{3.17}$$

We remark that (3.17) may be viewed as a generalization of the superconvergent boundary-flux calculation proposed by Carey et al. (1985).

The same technique can also be used to obtain approximate expressions for the interfacial normal $\mathbf{n}$ and total curvature K by postprocessing the approximate level set functions. Specifically, multiplying both sides of $(3.12)_1$ and $(3.12)_2$ by w_d and lumping quantities at the point $\mathbf{x}_d$, we obtain

$$\mathbf{n}^e(\mathbf{x}_d) \approx \frac{\int_{\mathcal{B}} \frac{\operatorname{Grad} \zeta}{|\operatorname{Grad} \zeta|} w_d \, \mathrm{d}v}{\int_{\mathcal{B}} w_d \, \mathrm{d}v} \tag{3.18}$$

and

$$K^e(\mathbf{x}_d) \approx \frac{\int_{\mathcal{B}} \frac{\operatorname{Grad} \zeta}{|\operatorname{Grad} \zeta|} \cdot \operatorname{Grad} w_d \, \mathrm{d}v}{\int_{\mathcal{B}} w_d \, \mathrm{d}v}. \tag{3.19}$$

3.4. Discretization with the XFE/LSM

3.4.1. Approximation for the motion y

Finite-element computations entail the projection of the solution space $\mathcal{A}_m$ and the associated space $\mathcal{V}_m$ of variations onto finite-dimensional subspaces $\mathcal{A}_m^h$ and $\mathcal{V}_m^h$. The Galerkin approximation of the variational boundary-value problem stated in Section 3.2.1 reads: find $\mathbf{y}^h$ in $\mathcal{A}_m^h$ such that

$$\sum_{\gamma=\alpha,\beta} \int_{\mathcal{R}_\gamma} \frac{\theta}{\theta_\gamma} \frac{\partial W_\gamma(\imath(\mathbf{B}^h))}{\partial \mathbf{F}^h} \cdot \operatorname{Grad} \mathbf{w}^h \, \mathrm{d}v = \int_{(\partial \mathcal{R})_t} \mathbf{s} \cdot \mathbf{w}^h \, \mathrm{d}a, \tag{3.20}$$

for all variations $\mathbf{w}^h$ of $\mathbf{y}^h$ belonging to $\mathcal{V}_m^h$.

We consider the set of overlapping subdomains $\{\Omega_i\}$ defining the support of each nodal shape function and an enrichment function r that possesses desirable approximation properties in a vicinity of the interface. The approximation for the deformation is given by

$$\mathbf{y}^h(\mathbf{x}, t) = \underbrace{\sum_{i \in I} \mathbf{c}_i(t) \phi_i(\boldsymbol{\xi}(\mathbf{x}))}_{\text{classical approximation}} + \underbrace{\sum_{j \in J} \mathbf{e}_j(t) \phi_j(\boldsymbol{\xi}(\mathbf{x})) r(\mathbf{x}, t)}_{\text{enrichment}}, \tag{3.21}$$

where ϕ_i, $i = 1, 2, \ldots$ are the nodal shape functions and $\boldsymbol{\xi}$ the local element coordinates. In the above, I denotes the set of all nodes in the mesh and $J = \{j \in I : \Omega_j \cap \mathcal{S} \neq \emptyset\}$ the set of nodes that form a partition of

unity for r (Melenk and Babuška, 1996). An example of a two-dimensional mesh with superimposed interface and the subset $J \subset I$ identified is shown in Fig. 3.

To capture the discontinuity in the gradient of the motion normal to the interface, we enrich with the "ridge" function (Moës et al., 2003)

$$r(\mathbf{x}) = \sum_i |\zeta_i| \phi_i(\boldsymbol{\xi}(\mathbf{x})) - \left| \sum_i \zeta_i \phi_i(\boldsymbol{\xi}(\mathbf{x})) \right|, \tag{3.22}$$

where ζ_i is the signed-distance function to the interface evaluated at the vertex of node i. As the discontinuity coincides with the phase interface, the above choice provides a mechanism for the approximation (3.21) to represent the geometry of the interface independent of the element boundaries. Furthermore, as the interface evolves, we update the enrichment function and the set J; no remeshing is performed.

Substitution of (3.21) into (3.20) results in a non-linear system of equations in $\{\mathbf{c}_i, \mathbf{e}_j\}$. We employ the standard Newton–Raphson procedure and solve the above with a sequence of linearized problems. These take the form

$$\mathbf{K}_f^{(n)} \Delta \mathbf{d}_f = \mathbf{r}^{(n)} \tag{3.23}$$

with $\mathbf{K}_f^n$ the tangent stiffness matrix at iteration n, r^n the residual vector, and $\Delta \mathbf{d}_f$ the vector gathering the incremental degrees of freedom $\Delta \mathbf{c}_i$ and Δe_j. After solving the above, the solution is updated in accord with $\mathbf{c}_i^{n+1} = \mathbf{c}_i^n + \Delta \mathbf{c}_i$ and $\mathbf{e}_j^{n+1} = \mathbf{e}_j^n + \Delta \mathbf{e}_j$.

The construction of the tangent stiffness matrix and residual vector requires the accurate integration of terms containing the classical and enriched basis functions over the element subdomains. The standard element-based quadrature routines are modified for those elements wherein the functions are discontinuous. Details can be found in Moës et al. (1999) and Dolbow et al. (in press).
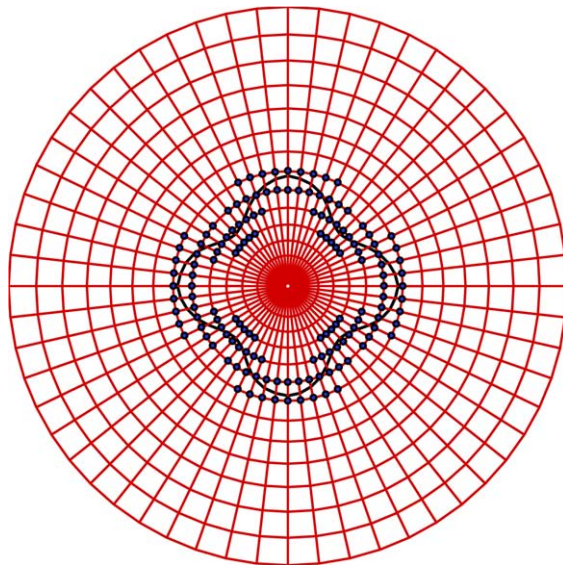

Fig. 3. Two-dimensional mesh of four-node quadrilateral elements with an interface $\mathcal{S}$ superimposed. The circled nodes correspond to the subset J that are enriched with the ridge function r to capture gradient discontinuities across the interface.

3.4.2. Approximation for the temperature θ

The Galerkin approximation to the variational boundary-value problem stated in Section 2 reads: find θ^h in $\mathcal{A}_\theta^h$ such that

$$\sum_{\gamma=\alpha,\beta} \int_{\mathcal{R}_\gamma} (\dot{\theta}^h w^h + k_\gamma \operatorname{Grad} \theta^h \cdot \operatorname{Grad} w^h) \, \mathrm{d}v + \int_{\mathcal{S}} \alpha^h \theta^h w^h \, \mathrm{d}a$$

$$= \sum_{\gamma=\alpha,\beta} \int_{\mathcal{R}_\gamma} s^h w^h \, \mathrm{d}v + \int_{(\partial\mathcal{R})_f} \bar{q} w^h \, \mathrm{d}a + \int_{\mathcal{S}} \alpha^h \theta_g^h w^h \, \mathrm{d}a \tag{3.24}$$

for all variations w^h of θ^h belonging to $\mathcal{V}_\theta^h$.

The approximation to the temperature field takes the form

$$\theta^h(\mathbf{x}, t) = \sum_{i \in I} a_i(t) \phi_i(\boldsymbol{\xi}(\mathbf{x})) + \sum_{j \in J} b_j(t) \phi_j(\boldsymbol{\xi}(\mathbf{x})) r(\mathbf{x}, t), \tag{3.25}$$

in which $\{\phi_i\}$ is the set of nodal shape functions used in the approximation for the motion. Here, enrichment with the ridge function allows the approximation θ^h to represent arbitrary gradient discontinuities in the temperature field across the interface.

We consider the solution on the time interval $[0, t_f]$, partitioned into time steps as $[t^n, t^{n+1}]$. We employ the backward Euler time-stepping algorithm to approximate $\dot{\theta}$:

$$\dot{\theta}^{n+1} = \frac{\theta^{n+1} - \theta^n}{\Delta t} \tag{3.26}$$

with $\Delta t = t^{n+1} - t^n$. This scheme is well-known to be first-order accurate and unconditionally stable. Substituting the above into (3.24) yields the semi-discrete Galerkin formulation at time t^{n+1}:

$$\sum_{\gamma=\alpha,\beta} \int_{\mathcal{R}_\gamma} \left(\frac{(\theta^{n+1})^h}{\Delta t} w^h + k_\gamma \operatorname{Grad} (\theta^{n+1})^h \cdot \operatorname{Grad} w^h \right) \mathrm{d}v + \int_{\mathcal{S}} \alpha^h (\theta^{n+1})^h w^h \, \mathrm{d}a$$

$$= \sum_{\gamma=\alpha,\beta} \int_{\mathcal{R}_\gamma} \left(\frac{(\theta^n)^h}{\Delta t} + s^h \right) w^h \, \mathrm{d}v + \int_{(\partial\mathcal{R})_f} \bar{q} w^h \, \mathrm{d}a + \int_{\mathcal{S}} \alpha^h (\theta_g^{n+1})^h w^h \, \mathrm{d}a. \tag{3.27}$$

We again adopt a Bubnov–Galerkin approximation and write approximations for the variations w^h in forms similar to (3.25). Upon substituting the approximations into the discrete weak form (3.27) and invoking the arbitrariness of the variations, we obtain a linear system of equations

$$\mathbf{K}_\theta d_\theta = f_\theta, \tag{3.28}$$

where d_θ gathers the degrees of freedom a_i and b_j.

We remark that α^h, θ_g^h and s^h in (3.27) are obtained upon substitution of $\mathbf{y}^h$ and θ^h into (3.6) and (3.8). A backward Euler algorithm is employed to calculate $\dot{\mathbf{F}}$ from $\mathbf{y}(t^{n+1})$ and $\mathbf{y}(t^n)$. In the present operator split, we use the approximate temperature field θ^h employed in the previous thermal step to calculate these quantities. Otherwise, (3.27) would represent a non-linear system of equations for the degrees of freedom d_θ. Through iteration between *Stage I* and *Stage II*, convergence in both the approximate motion and temperature fields is obtained.

3.5. Discrete versions of domain integrals

We use discrete forms of the domain integrals discussed in Section 3.3.1 that do not employ an ambiguous "domain size multiplier". This is to be contrasted with well-known domain integral techniques for fracture mechanics (Moran and Shih, 1987).

Consider the set of nodes $D = \{i \in I : \Omega_i \cap \mathbf{x}_d \neq \emptyset\}$ whose support contains the point $\mathbf{x}_d$. The contribution e_k of node $k \in D$ to the mechanical driving traction at a point $\mathbf{x}_d$ on the interface is given by

$$\mathsf{e}_k(\mathbf{x}_d) = -\frac{\sum_{\gamma=\alpha,\beta} \int_{\mathcal{Q}_\gamma^e \in \Omega_k} \mathbf{n}^h \cdot \mathbf{E}_\gamma(\theta^h, \operatorname{Grad} \mathbf{y}^h) \operatorname{Grad} \phi_k \, dv}{\int_{\mathcal{L}^h} \phi_k \, da}. \tag{3.29}$$

Repeating the above calculation for each node in the set D allows us to construct the approximation

$$\mathsf{e}^h(\mathbf{x}_d) = \sum_{i \in D} \mathsf{e}_i(\mathbf{x}_d) \phi_i(\boldsymbol{\xi}(\mathbf{x}_d)). \tag{3.30}$$

In effect, only those nodes with support containing the point x_d contribute to the domain integral approximation to e.

The above expression involves an approximation $\mathbf{n}^h$ to the extended normal $\mathbf{n}^e$ obtained from the level-set function ζ. Consistent with the above, we use

$$\mathbf{n}^h(\mathbf{x}_d) = \sum_{i \in D} \mathbf{n}_i^e(\mathbf{x}_d) \phi_i(\boldsymbol{\xi}(\mathbf{x}_d)), \tag{3.31}$$

where the coefficients $\mathbf{n}_i^e(\mathbf{x}_d)$ denote lumped approximations to the extended normal. For the approximation K^h to the curvature appearing in the Galerkin approximation (3.24) to u, we likewise take

$$\mathsf{K}^h(\mathbf{x}_d) = \sum_{i \in D} \mathsf{K}_i^e \mathbf{x}_d \phi_i(\boldsymbol{\xi}(\mathbf{x}_d)) \tag{3.32}$$

with the constants $\mathsf{K}_i^e(\mathbf{x}_d)$ denoting lumped approximations to the extended curvatures at the nodes. The coefficients $\mathbf{n}_i^e(\mathbf{x}_d)$ and $\mathsf{K}_i^e(\mathbf{x}_d)$ are both determined using the approximation ζ^h to the level-set function ζ, as described in the next section.

The discrete domain integral approximation to the jump in normal component of the heat flux is given similarly by

$$\mathsf{j}^h(\mathbf{x}_d) = \sum_{i \in D} \mathsf{j}_i(\mathbf{x}_d) \phi_i(\boldsymbol{\xi}(\mathbf{x}_d)) \tag{3.33}$$

with

$$\mathsf{j}_k(\mathbf{x}_d) = -\frac{\sum_{\gamma=\alpha,\beta} \sum_e \int_{\mathcal{Q}_\gamma^e \in \Omega_k} (\dot{\theta}^h \phi_k - s^h \phi_k + k_\gamma \operatorname{Grad} \theta^h \cdot \operatorname{Grad} \phi_k) \, dv}{\int_{\mathcal{L}^h} \phi_k \, da}. \tag{3.34}$$

The expression (3.6)₂ for p does not lend itself to evaluation with domain integrals because it is difficult to identify a corresponding bulk equation. Therefore, we employ the direct evaluation

$$\mathsf{p}^h = \left[\!\!\left[\frac{\theta}{\theta_\gamma} \frac{\partial W_\gamma(\iota(\mathbf{B}^h))}{\partial \mathbf{F}^h} \mathbf{n}^h \cdot \mathbf{F}^h \mathbf{n}^h \right]\!\!\right]. \tag{3.35}$$

3.6. Level-set algorithm and coupling with bulk fields

We write $\mathcal{A}_\zeta^h$ for the finite-dimensional subspace of $\mathcal{A}_\zeta$, and approximate $\dot{\zeta}$ using the forward Euler algorithm

$$\dot{\zeta}^n = \frac{\zeta^{n+1} - \zeta^n}{\Delta t}, \tag{3.36}$$

substituting into (3.14), this yields: find $(\zeta^{n+1})^h \in \mathcal{A}_\zeta^h$ such that

$$\int_\mathcal{R} (\zeta^{n+1})^h w^h \, \mathrm{d}v = \int_\mathcal{R} (\zeta^n)^h w^h \, \mathrm{d}v - \Delta t \int_\mathcal{R} (v^e)^h w^h \, \mathrm{d}v \tag{3.37}$$

for all $w^h \in \mathcal{A}_\zeta^h$.

We approximate ζ using the same nodal shape functions that were employed for the motion and temperature fields:

$$\zeta^h = \sum_{i \in I} \zeta_i(t) \phi_i(\boldsymbol{\xi}(\mathbf{x})). \tag{3.38}$$

Enrichment is not used since we anticipate ζ to be smooth in the vicinity of the interface.

Substituting (3.38) (and an analogous expansion for w^h) into (3.37), and lumping quantities at the nodes yields the simple update formula

$$\zeta_i^{n+1} = \zeta_i^n - \Delta t v^e(\mathbf{x}_i). \tag{3.39}$$

The key to the algorithm concerns the construction of the extension velocity v^e. In particular, we seek to construct the extension velocity such that the solution to (3.13) is the signed distance function to the interface. A standard approach (Sethian, 1999) is to construct v^e such that

$$v^e|_{\zeta=0} = \mathsf{v}, \quad \text{and} \quad \operatorname{Grad} v^e \cdot \operatorname{Grad} \zeta = 0. \tag{3.40}$$

Fast marching methods have been developed to effect this, but a simpler approach suggested in Garikipati and Rao (2001) is followed here.

The normal velocity v is first determined on each subsurface $\mathcal{S}^e$ through a discrete form of $(2.24)_2$:

$$\mathsf{v}^h = -\frac{j^h}{\ell - \mathsf{p}^h + \sigma \mathsf{K}^h} \tag{3.41}$$

incorporating the aforementioned domain-integral approximation (3.33) to the jump in heat flux. We then loop over the nodes in the mesh and determine the closest point projection $\mathbf{x}_p$ of each vertex $\mathbf{x}_i$ onto the interface as represented by the set of subsurfaces $\{\mathcal{S}^e\}$. The extension velocity at the node is then assigned via

$$v^e(\mathbf{x}_i) = \mathsf{v}^h(\mathbf{x}_p(\mathbf{x}_i)). \tag{3.42}$$

We use bilinear shape functions based upon standard four-node quadrilateral elements. Substitution of (3.38) directly into (3.12) leads to expressions for $\mathbf{n}^e$ and K^e that are nearly constant or vanish over each element $\mathcal{Q}_e$. The extended normal and total curvature are much more accurately approximated using discrete versions of (3.18) and (3.19), respectively. Thus, about each vertex in the vicinity of the interface we calculate

$$\mathbf{n}_i^e = \frac{\int_{\mathcal{Q}_e \in \Omega_i} \frac{\operatorname{Grad} \zeta^h}{|\operatorname{Grad} \zeta^h|} \phi_i \, \mathrm{d}v}{\int_{\mathcal{Q}_e \in \Omega_i} \phi_i \, \mathrm{d}v} \tag{3.43}$$

and

$$\mathsf{K}_i^e = \frac{\int_{\mathcal{Q}_e \in \Omega_i} \frac{\operatorname{Grad} \zeta^h}{|\operatorname{Grad} \zeta^h|} \cdot \operatorname{Grad} \phi_i \, \mathrm{d}v}{\int_{\mathcal{Q}_e \in \Omega_i} \phi_i \, \mathrm{d}v} \tag{3.44}$$

for use in the expansions (3.31) and (3.32). In Dolbow et al. (in press), we demonstrated that the foregoing approximations are second-order accurate.

3.7. Staggered solution strategy

To find an accurate solution to the transient problem, it is necessary to perform an iterative strategy at each time-step. We use $(\cdot)^{n,k}$ to denote values at iteration k within time step n, and $(\cdot)^n$ for the converged solution of time-step n.

The following strategy assumes that all fields are known at time-step n, and the objective is to obtain the converged fields at time-step $n + 1$.

1. Set $t^{n+1} = t^n + \Delta t$. At time-step $n + 1$, evolve the interface geometry by updating the coefficients ζ_i through (3.39).
2. Start iterations in time-step $n + 1$ with $k = 0$.
   (a) If $k = 0$, set $\theta^{n+1,0} = \theta^n$ and $v^{n+1,0} = v^n$. Solve the force balance equations (3.23) with $\theta = \theta^{n+1,k}$. Postprocess the mechanical fields to obtain e^h and p^h given by (3.30) and (3.35) and then determine α and θ_g, s through (3.6) and (3.8), respectively.
   (b) With α, θ_g, and s known, solve (3.27) to obtain $\theta^{n+1,k+1}$.
   (c) Determine the approximate velocity $v^{n+1,k+1}$ using (3.41) and then evaluate the error norm

$$\sqrt{\frac{\int_{\mathcal{S}}(v^{n+1,k+1} - v^{n+1,k})^2 \, da}{\int_{\mathcal{S}}(v^{n+1,k+1})^2 \, da}}.$$

   (d) Compare the error norm to a tolerance ϵ_v. If the error norm is larger than ϵ_v, set $k = k + 1$, go back to step (a) and repeat steps (a)–(d). Otherwise, set $\theta^{n+1} = \theta^{n+1,k+1}$ and $v^{n+1} = v^{n+1,k+1}$.
3. Return to step 1.

4. Application: swelling of a spherical specimen

We first consider a spherical gel specimen with a traction-free boundary occupying the region

$$\mathcal{R} = \{\mathbf{x} : |\mathbf{x}| \leqslant R\} \tag{4.1}$$

with the temperature held spatially constant on its surface.

4.1. Kinematical specialization

We write

$$\mathbf{e} = \frac{\mathbf{x}}{|\mathbf{x}|} \tag{4.2}$$

for the base vector. The requirement that the specimen be traction-free yields

$$\mathbf{Se}|_{\partial \mathcal{R}} = \mathbf{0}. \tag{4.3}$$

Writing Θ for the time-dependent temperature at the boundary of the specimen, we have

$$\theta|_{\partial \mathcal{R}} = \Theta. \tag{4.4}$$

We restrict attention to circumstances in which the deformation and the temperature depend at most on radial position $r = |\mathbf{x}|$ and time t, viz.,

$$\mathbf{y}(\mathbf{x},t) = y(r,t)\mathbf{e} \quad \text{and} \quad \theta(\mathbf{x},t) = \theta(r,t). \tag{4.5}$$

Consistent with these assumptions, we suppose that the interface is spherical, and write

$$\mathcal{S}(t) = \{\mathbf{x} : |\mathbf{x}| = \mathsf{s}(t)\} \tag{4.6}$$

for its position at time t. Anticipating that swelling should proceed from the boundary inward toward the center of the specimen,

$$\mathbf{n} = -\mathbf{e}, \qquad \mathsf{K} = -\mathrm{Grad}_S\mathbf{n} = \frac{2}{\mathsf{s}}, \quad \text{and} \quad \mathsf{v} = -\dot{\mathsf{s}}. \tag{4.7}$$

We use g' to denote the partial derivative of a field g with respect to r. Thus, by $(4.5)_1$, the deformation gradient has the particular form

$$\mathbf{F}(r,t) = y'(r,t)\mathbf{e}\otimes\mathbf{e} + \frac{y(r,t)}{r}(\mathbf{I} - \mathbf{e}\otimes\mathbf{e}) \tag{4.8}$$

and the Jacobian is given by

$$J(r,t) = \det\mathbf{F}(r,t) = \frac{y^2(r,t)y'(r,t)}{r^2} > 0. \tag{4.9}$$

4.2. Reduced evolution equations

4.2.1. Bulk equations
In view of (2.5) and (4.8), and (4.9), the stress field is given by

$$\mathbf{S}(\mathbf{F},\theta) = \frac{\partial\Psi_\gamma(\mathbf{F},\theta)}{\partial\mathbf{F}} = S_\parallel\mathbf{e}\otimes\mathbf{e} + S_\perp(\mathbf{I} - \mathbf{e}\otimes\mathbf{e}) \tag{4.10}$$

with

$$S_\parallel(r,t) = \left(\mu_\gamma\left(y'(r,t) - \frac{J_\gamma^{\frac{2}{3}}}{y'(r,t)}\right) + \frac{\lambda_\gamma J_\gamma^{\frac{2}{3}}D(r,t)}{2y'(r,t)}\right)\frac{\theta}{\theta_\gamma} \tag{4.11}$$

and

$$S_\perp(r,t) = \left(\mu_\gamma\left(\frac{y(r,t)}{r} - \frac{J_\gamma^{\frac{2}{3}}r}{y(r,t)}\right) + \frac{\lambda_\gamma J_\gamma^{\frac{2}{3}}rD(r,t)}{2y(r,t)}\right)\frac{\theta}{\theta_\gamma} \tag{4.12}$$

the components of radial and hoop stress, with

$$D(r,t) = \frac{J(r,t)}{J_\gamma}\left(\frac{J(r,t)}{J_\gamma} - 1\right) + \log\left(\frac{J(r,t)}{J_\gamma}\right). \tag{4.13}$$

The deformational force balance $(3.1)_1$ reduces to the scalar equation $(r^2 S_\parallel(r,t))' = 2rS_\perp(r,t)$, which, by (4.11) and (4.12), can be written as

$$\left(\frac{\theta}{\theta_\gamma}\left(\mu_\gamma r^2\left(y'(r,t) - \frac{J_\gamma^{\frac{2}{3}}}{y'(r,t)}\right) + \frac{\lambda_\gamma J_\gamma^{\frac{2}{3}}r^2 D(r,t)}{2y'(r,t)}\right)\right)'$$

$$= 2\left(\mu_\gamma\left(y(r,t) - \frac{J_\gamma^{\frac{2}{3}}r^2}{y(r,t)}\right) + \frac{\lambda_\gamma J_\gamma^{\frac{2}{3}}r^2 D(r,t)}{y(r,t)}\right)\frac{\theta}{\theta_\gamma}. \tag{4.14}$$

Similarly, by $(4.5)_2$, the heat conduction equation $(3.2)_2$ simplifies to

$$r^2 \dot{\theta}(r,t) = k_\gamma (r^2 \theta'(r,t))' + S_\parallel(r,t)\dot{y}'(r,t) + 2S_\perp(r,t)\frac{\dot{y}(r,t)}{r}. \tag{4.15}$$

4.2.2. Interfacial equations

On appealing to $(4.7)_1$ and (4.10), the deformational force balance $(2.24)_1$ at the interface reduces to the scalar equation $[\![S_\parallel]\!] = 0$, which, by (4.11), can be written as

$$\left[\!\!\left[\frac{\theta}{\theta_\gamma}\left(\mu_\gamma \left(y'(\mathsf{s}(t),t) - \frac{J_\gamma^{\frac{2}{3}}}{y'(\mathsf{s}(t),t)} \right) + \frac{\lambda_\gamma J_\gamma^{\frac{2}{3}} D(\mathsf{s}(t),t)}{2y'(\mathsf{s}(t),t)} \right) \right]\!\!\right] = 0. \tag{4.16}$$

Similarly, by (4.5) and $(4.7)_{1,3}$, the expression for the interfacial velocity $(2.24)_2$ simplifies to

$$\dot{\mathsf{s}}(t) = \frac{[\![k_\gamma \theta'(\mathsf{s}(t),t)]\!]}{\ell - S_\parallel(\mathsf{s}(t),t)[\![y'(\mathsf{s}(t),t)]\!] + \frac{2\sigma}{\mathsf{s}(t)}}. \tag{4.17}$$

Finally, by (2.11), (4.8), (4.10), (4.11), (4.12), and (4.7), the normal configurational force balance $(2.24)_3$ becomes

$$\theta_s(t) = -\frac{\frac{2\sigma}{\mathsf{s}(t)} + \frac{\dot{\mathsf{s}}(t)}{M} + \ell + \mathsf{e}(\mathsf{s}(t),t)}{[\![\log\theta_\gamma]\!]}, \tag{4.18}$$

where $\theta_s(t) = \theta(\mathsf{s}(t),t)$, and where $\mathsf{e}(\mathsf{s}(t),t) = \theta(\mathsf{s}(t),t)[\![E_\parallel(\mathsf{s}(t),t)]\!]$, with

$$[\![E_\parallel(\mathsf{s}(t),t)]\!] = -\frac{1}{2}\left[\!\!\left[\frac{\mu_\gamma}{\theta_\gamma}\left((y'(\mathsf{s}(t),t))^2 + \frac{2y^2(\mathsf{s}(t),t)}{\mathsf{s}^2(t)} + 2J_\gamma^{\frac{2}{3}}\log\left(\frac{J(\mathsf{s}(t),t)}{J_\gamma}\right) - 3J_\gamma^{\frac{2}{3}} \right) \right]\!\!\right]$$
$$+ \frac{1}{4}\left[\!\!\left[\frac{\lambda_\gamma}{\theta_\gamma} J_\gamma^{\frac{2}{3}}\left(\left(\frac{J(\mathsf{s}(t),t)}{J_\gamma} - 1\right)^2 + \log^2\left(\frac{J(\mathsf{s}(t),t)}{J_\gamma}\right) - 6D(\mathsf{s}(t),t) \right) \right]\!\!\right]. \tag{4.19}$$

4.2.3. Boundary conditions

Consistent with the assumed symmetry of the deformation, we have the condition

$$y(0,t) = 0 \tag{4.20}$$

at the center of the specimen. By (4.10), considering $\theta > 0$, the traction-free condition (4.3) reduces to

$$\mu_\alpha\left(y'(R,t) - \frac{J_\alpha^{\frac{2}{3}}}{y'(R,t)} \right) + \frac{\lambda_\alpha J_\alpha^{\frac{2}{3}} J(R,t)}{2y'(R,t)} = 0. \tag{4.21}$$

The requirement that θ be radially symmetric implies

$$\theta'(0,t) = 0. \tag{4.22}$$

By $(4.5)_2$, (4.4) becomes

$$\theta(R,t) = \Theta(t). \tag{4.23}$$

4.2.4. Initial condition

We suppose that the position of the interface is given initially, so that

$$\mathsf{s}(0) = \mathsf{s}_0, \quad \text{with } 0 \leqslant \mathsf{s}_0 \leqslant R. \tag{4.24}$$

4.3. Numerical investigation

The thermomechanical model is similar to the chemo-mechanical problem presented in Dolbow et al. (2004) in many ways, albeit with stronger coupling between the bulk fields. In the following numerical studies, we focus on some of the more unique predictions provided by the thermomechanical model. We perform all studies using a mesh with uniform nodal spacing $h = R/100$, which was found to yield converged results.

4.3.1. Steady-state solution

Under steady-state conditions, $\dot{\theta} = 0$, $\dot{y} = 0$, $\dot{s} = 0$, and the governing equations simplify considerably. Further, a spatially constant temperature field Θ_{ss} satisfies the bulk equation (4.15). For such a constant-temperature state to exist with the position s of the interface located in the open interval between $r = 0$ and $r = R$ and satisfy both the interface condition (4.18) and the boundary condition (4.23), we must have

$$\theta(r) = \theta(s) = \Theta_{ss} \tag{4.25}$$

for all r in $(0, R)$, with

$$\Theta_{ss} = -\frac{\frac{2\sigma}{s} + \ell}{[\![\log \theta_\gamma]\!] + [\![E_\parallel]\!]}, \tag{4.26}$$

where the mechanical contribution $E_\parallel$ is given in terms of the motion y by (4.19). We note that when the temperature is spatially uniform, the solution y to the bulk force balance (4.14) is independent of θ. For a given position of the interface, the force balance equations can be solved, yielding $E_\parallel$ and a steady-state temperature Θ_{ss} through (4.26).

We next examine the variation in this steady-state temperature for a sequence of interface positions. The material properties used in these tests are given in Table 1. The normalized steady-state temperature is shown in Fig. 4 as a function of normalized interface position. As the interface position is increased, the collapsed phase occupies an increasingly greater portion of the domain and the steady-state temperature is found to decrease.

Table 1
Baseline material properties and parameters used in the parametric studies

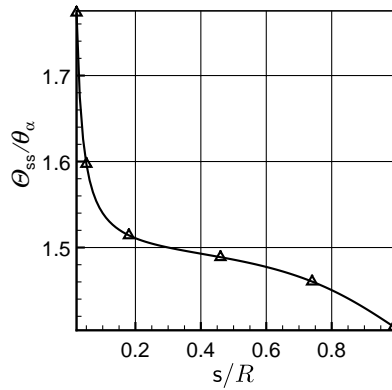| Property	Normalization	Collapsed phase (β)	Swollen phase (α)
c	c	1.0	1.0
k_γ	$\dfrac{k_\gamma T}{c\theta_\alpha Z^2}$	0.01	0.02
θ_γ	$\dfrac{\theta_\gamma}{\theta_\alpha}$	0.5	1.0
σ	$\dfrac{\sigma}{c\theta_\alpha Z}$	0.002	0.002
M	$\dfrac{Mc\theta_\alpha T}{Z}$	500	500
μ_γ	$\dfrac{\mu_\gamma}{c\theta_\alpha}$	0.005	0.0025
λ_γ	$\dfrac{\lambda_\gamma}{c\theta_\alpha}$	0.025	0.005
J_γ	J_γ	1.0	10.0
l	$\dfrac{l}{c\theta_\alpha}$	1.0	1.0

Fig. 4. Normalized steady-state temperature as a function of normalized interface position.

In light of (4.26) and examining the contribution from the latent heat with the material properties given in Table 1, we obtain $-\ell/[\![\log\theta_\gamma]\!] = -1/\log(0.5) = 1.443$. This level is close to the mean of the steady-state temperature profile shown in Fig. 4, and we find that it is the dominant factor in (4.26).

Since ℓ and $[\![\log\theta_\gamma]\!]$ are constants, the variation in Θ_{ss} with interface position is only determined by the interfacial tension σ and the quantity $[\![E_\parallel]\!]$. To quantify these influences, we examine the steady-state temperature by alternately setting $\sigma = 0$ or $[\![E_\parallel]\!] = 0$. The comparisons of these results to those obtained with non-zero σ and $[\![E_\parallel]\!]$ are shown in Fig. 5. We observe that $[\![E_\parallel]\!]$ dominates the variation in Θ_{ss} with s until the interface approaches the center of the specimen. Near the center of the specimen, the term $2\sigma/$s dominates due to the increased curvature of the interface.

We remark that, contrary to experimental observations, the steady-state temperature profiles indicate that the collapsed phase is preferred at lower temperatures than the swollen phase. This trend depends on the particular chosen values of material parameters. Alternative choices from those provided in Table 1 yield the reverse, i.e. steady-state temperature profiles that increase monotonically with s. However, we find that the material properties and parameters in Table 1 do yield *transient solutions* in accord with experimental observations, as discussed subsequently. We have not identified a set of material properties and parameters that yield the "correct" trend for both steady-state and transient solutions. These results suggest that the two-phase steady-state results are unstable.
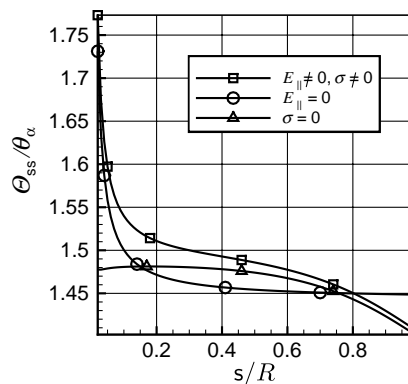

Fig. 5. Normalized steady-state temperature as a function of normalized interface position, with and without the interfacial free-energy density σ or the term $[\![E_\parallel]\!]$.

4.3.2. Transient solution

Next, we apply the iterative strategy described in Section 3.7 to obtain transient solutions to the coupled problem. We examine the swelling kinetics of a specimen with the following initial and boundary conditions

$$\mathsf{s}(0) = \mathsf{s}_0, \quad \theta(r,0) = \Theta_{ss}(\mathsf{s}_0) \quad \Theta(t) = \Theta_{ss}(\mathsf{s}_0) + \alpha H(t) \tag{4.27}$$

with H the Heaviside function, s_0 the initial position of the interface, and $\Theta_{ss}(\mathsf{s}_0)$ the steady-state temperature obtained from (4.26) at $\mathsf{s} = \mathsf{s}_0$. These conditions correspond to an initially equilibrated specimen that is subjected to a sudden change in boundary temperature. All numerical studies are performed on a mesh with mesh size $h = R/100$ and variable time steps $\Delta t = h/\mathsf{v}$.

We first examine the case in which the initial position of the interface ($\mathsf{s}_0 = 0.99R$) is close to the boundary and the specimen is nearly fully collapsed. To ensure full swelling, we also fix the boundary temperature to be $\Theta = 1.0$. Fig. 6 shows the normalized temperature at various time steps corresponding to incremental interface positions $\mathsf{s}/R = 0.8, 0.6, 0.4, 0.2$. Next, to examine the response of a gel specimen that is nearly fully swollen, we perform another set of tests with $\mathsf{s}_0 = 0.01R$. To ensure full collapse, we set the boundary temperature to $\Theta = 2.5$.

In Fig. 7, we superimpose the plots of the interfacial temperature from the two transient studies and the steady-state profile. We observe that the transition from a collapsed to a swollen state results in interfacial
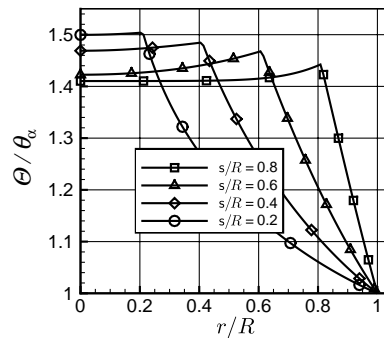

Fig. 6. Normalized temperature at various time steps corresponding to incremental interfacial positions as a gel specimen transitions from a swollen to a collapsed state.
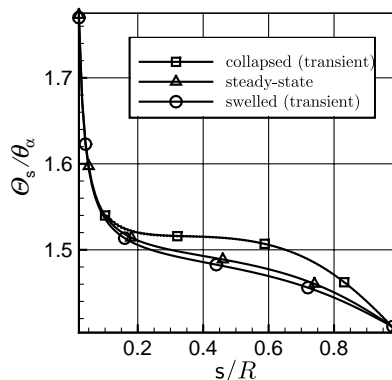

Fig. 7. Normalized interfacial temperature with interface position. Transient results for initially collapsed and swollen gel specimen are shown along with the steady-state profile.

temperatures that are greater than the steady-state levels. By contrast, the transition from a swollen to a collapsed state results in interfacial temperatures lower than the steady-state levels.

The evolution of the interfacial position and velocity with time for the swollen-to-collapsed transition are shown in Figs. 8 and 9. We note that in contrast to the collapsed-to-swollen transition (where the interface position is initially near the specimen boundary), there exists a slight temporal delay in the phase transition in response to the step change in boundary temperature. During this period the velocity of the interface is negligible and the thermal response is dominated by diffusion with very little deviation from the initial state.

We use the above process to identify transition temperatures $\theta_s^{\min}$ and $\theta_s^{\max}$. If the boundary temperature is below $\theta_s^{\min}$, an initially collapsed specimen will become fully swollen. On the other hand, if the boundary temperature is above $\theta_s^{\max}$, an initially swollen specimen will become fully collapsed. In Fig. 10 we show the variation of the steady-state swelling ratio

$$Q = \frac{y^3(R)}{R^3} \tag{4.28}$$

with the boundary temperature. The transition temperatures are different, which qualitatively agrees with the experimentally observed hysteresis for the volume transition (Hirokawa and Tanaka, 1984; Matsuo and Tanaka, 1988).
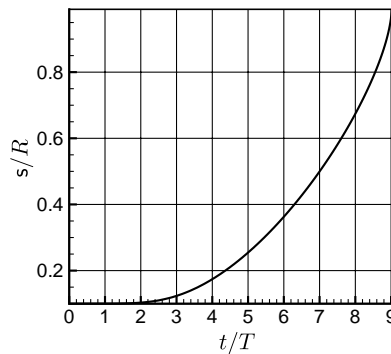

Fig. 8. Evolution of the interface position with time for an initially swollen gel specimen.
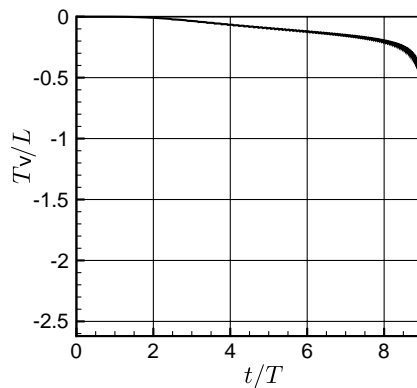

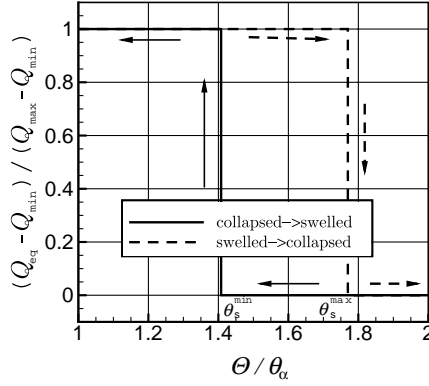Fig. 9. Normalized interfacial velocity as a function of time for an initially swollen gel specimen.

Fig. 10. Volume transition curves for the thermomechanical problem. The normalized transition temperature for the collapsed → swollen phase transition is identified as θ_s^{min} and that for the swollen → collapsed phase transition is θ_s^{max}.

4.3.3. Comparison with experimental observations

Experiments by Matsuo and Tanaka (1988) showed a hysteresis in the volume-phase transition in PNIPA hydrogels. The upper transition temperature, above which a swollen gel collapses with increasing temperature was found to be greater than the transition temperature for the reverse transition. Both temperatures were found to be between 33 °C and 38 °C for NIPA gels, with an average hysteresis gap around 3 °C. Shibayama et al. (1996) also reported a transition temperature of 32 °C for a NIPA hydrogel.

If we assume that the gel specimens are initially at room temperature, the results shown in Fig. 10 predict a hysteresis gap around 30 °C. Therefore, some adjustment to the material properties seems to be necessary to correlate our model with experimental observations. From our initial studies into the transient response, we observed only small deviations in the interfacial temperature from steady-state levels. Further, we find that the transition temperatures θ_s^{min} and θ_s^{max} correspond quite well to the minimum and maximum temperatures obtained from the steady-state profile.

Fig. 11 shows the steady-state interfacial temperature obtained after scaling the mechanical properties by 1/50 and σ by 1/2 from those given in Table 1. This gives rise to a hysteresis gap on the order of a few degrees as well as transition temperatures that compare quite well with the aforementioned experimental
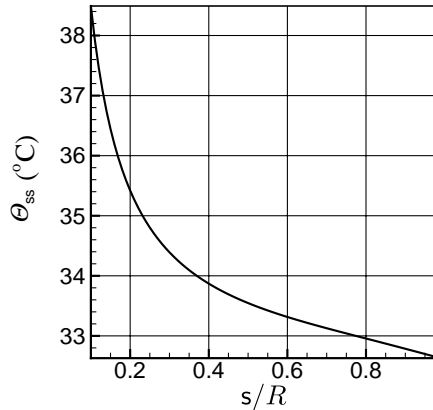

Fig. 11. Steady-state interfacial temperature with adjusted material properties.

observations. With the adjusted material properties, we note that the mechanical driving traction is relatively small and that the surface tension dominates the variation in Θ_{ss} with s.

5. Swelling of a cylindrical specimen

In this section, we examine the kinetic response of a cylindrical gel specimen with circular cross-section of radius R. Specifically, we choose a fixed orthonormal basis $\{\mathbf{e}_1, \mathbf{e}_2, \mathbf{e}_3\}$, write $x_i = \mathbf{x} \cdot \mathbf{e}_i$,

$$r = \sqrt{x_1^2 + x_2^2}, \quad \phi = \arctan\left(\frac{x_2}{x_1}\right) \tag{5.1}$$

and consider a reference state in which the medium occupies the cylindrical region

$$\mathcal{R} = \{\mathbf{x} : r \leqslant R, \quad -\infty < x_3 < \infty\}. \tag{5.2}$$

We assume that the deformation is a plane strain, so that

$$\mathbf{y}(\mathbf{x}, t) = y_1(x_1, x_2, t)\mathbf{e}_1 + y_2(x_1, x_2, t)\mathbf{e}_2 + x_3\mathbf{e}_3, \tag{5.3}$$

that the temperature field is independent of the axial coordinate, so that

$$\theta(\mathbf{x}, t) = \theta(x_1, x_2, t) \tag{5.4}$$

and that the lateral surface of the specimen is traction-free. Thus, introducing $\mathbf{e} = \cos\phi\mathbf{e}_1 + \sin\phi\mathbf{e}_2$, we have

$$\mathbf{Se} = \mathbf{0}. \tag{5.5}$$

The material properties are taken as given in Table 1. Annular meshes of four-node quadrilateral elements, such as the one shown in Fig. 3, are used throughout.

5.1. Self-similar interface evolution

First, we examine the case of a circular interface centered about the axis of the specimen, i.e.

$$\mathcal{S} = \{\mathbf{x} : |\mathbf{x}| = r_{\text{s}}\} \tag{5.6}$$

with $r_{\text{s}} < R$.

In the first set of studies, we fix the interface geometry as cylindrical at equally spaced radii and compute the steady-state solution at these locations. Fig. 12 shows the steady-state temperature obtained on a series of meshes with various levels of resolution. A 10×40 mesh, for example, uses 10 elements in the radial direction and 40 in the circumferential direction. The results indicate that converged results are obtained even on a relatively coarse mesh.

Next, we neglect the mechanical contributions to the interfacial conditions and seek the transient solution of the decoupled thermal problem. In this case, the interfacial temperature and velocity are given by

$$\theta_s = \frac{\mathsf{v}/M - \ell - \sigma\mathsf{K}}{[\![\log\theta_\gamma]\!]} \tag{5.7}$$

and

$$\mathsf{v} = -\frac{[\![k_\gamma\mathrm{Grad}\theta]\!] \cdot \mathbf{n}}{\ell + \sigma\mathsf{K}}. \tag{5.8}$$

The initial conditions and are taken as

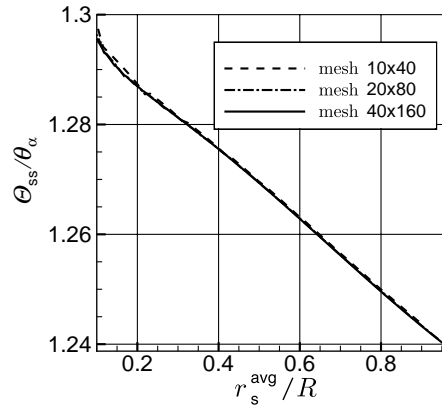$$r_s(0) = 0.975R, \quad \theta(0) = \Theta_{\text{ss}}(r_s(0)) \tag{5.9}$$

Fig. 12. Normalized steady-state temperature as a function of normalized interface position for a cylindrical specimen.

with the boundary condition

$$\Theta = 1.2. \tag{5.10}$$

We compare the results of a decoupled thermal problem to those of the fully coupled problem. The comparisons of the interfacial position and velocity are shown in Figs. 13 and 14, respectively. We note that the total swelling time is longer for the fully coupled system which shows that the mechanical contribution acts to retard the evolution of the interface and thus the phase transition. The evolution of the interface position with time takes a sigmoidal shape, but we note that velocity of the interface is nearly constant over a large percentage of the transition time.

5.2. Perturbed interface evolution

We next investigate the conditions for unstable growth of the interface by perturbing its initial geometry. For illustrative purposes, we use

$$\mathcal{S}(0) = \{\mathbf{x} : r = r_s + p\cos(n\phi)\} \tag{5.11}$$
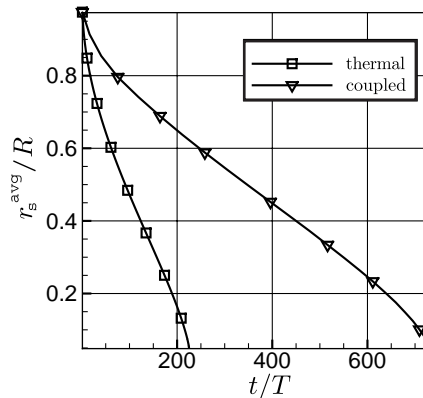

Fig. 13. Evolution of normalized interfacial position with time. Results are obtained by solving a purely thermal and a fully coupled system.
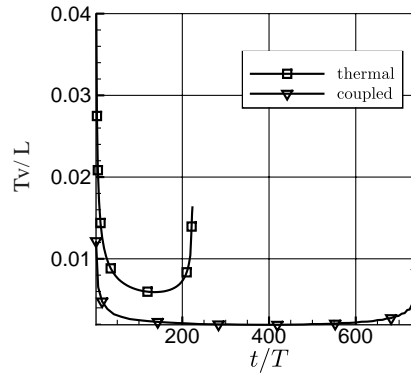
Fig. 14. Evolution of normalized interfacial velocity with normalized time. Results are shown for a purely thermal and a fully coupled system.

with $r_s/R = 0.2$, $p/R = 0.01$, and $n = 5$ (corresponding to a 5%, five-fold symmetric perturbation of a circular interface centered about the axis of the specimen). We take the temperature on the boundary of
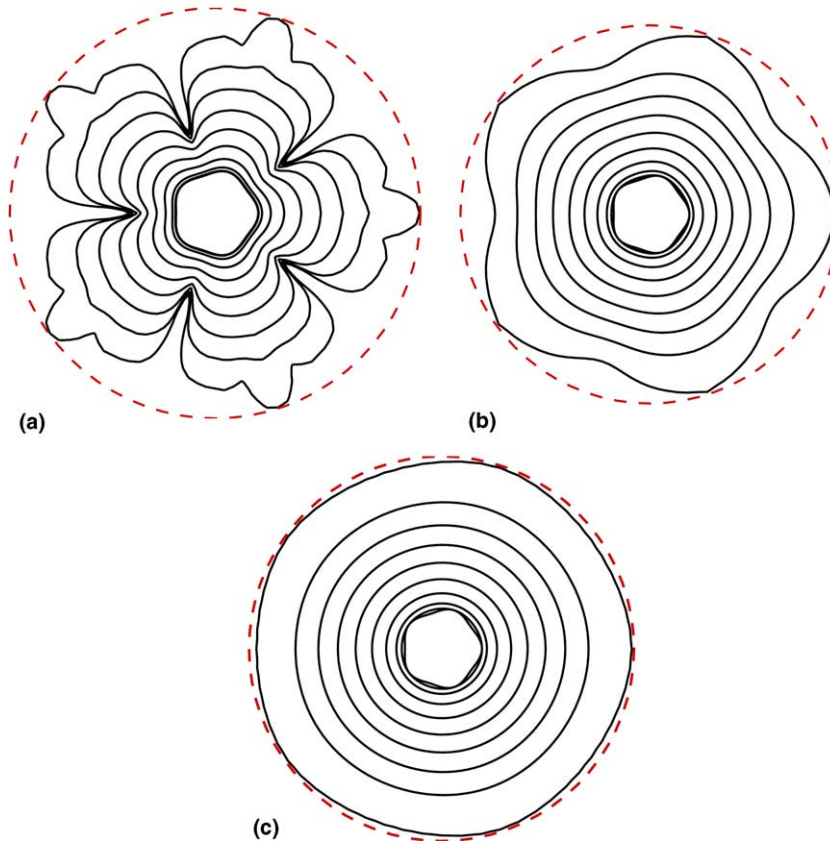

Fig. 15. Interface evolution in the reference configuration for various magnitudes of the normalized interfacial free-energy density σ. The dashed lines denote the surface of the gel specimen in the reference configuration. (a) $\sigma/c\theta_\alpha L = 0.0002$, $\Delta t/T = 7.96$. (b) $\sigma/c\theta_\alpha L = 0.002$, $\Delta t/T = 8.70$. (c) $\sigma/c\theta_\alpha L = 0.004$, $\Delta t/T = 8.92$.

the specimen to be $\Theta = 2.0$. As a result, the interface evolves toward the free surface of the specimen while the swollen phase transitions to the collapsed phase. For the chosen values, we find that a 30×120 mesh yields sufficiently converged results.

We investigate the influence of the interfacial free-energy density σ on the evolution of the interface. In order to show more influence of the change of surface tension on the unstable growth of the interface, we scale the mechanical parameters μ_γ and λ_γ by 1/100. We also decrease the interfacial mobility to $M = 1.0$ to stabilize the front in the case when a relatively small σ is used. The results are presented in Fig. 15 for various magnitudes of the dimensionless interfacial free-energy density σ with the other dimensionless material parameters fixed at those given in Table 1. In each case, the geometry of the interface in the reference configuration is shown at equally spaced time intervals. For a relatively small magnitude of $\sigma = 0.0002$, the perturbation of the interface is observed to increase with time. Larger values of the interfacial free-energy density both decrease the average velocity of the interface and stabilize the perturbation. The results indicate the sensitivity of the interface evolution to the interfacial free-energy density, a phenomena commonly observed in other processes such as dendritic solidification.
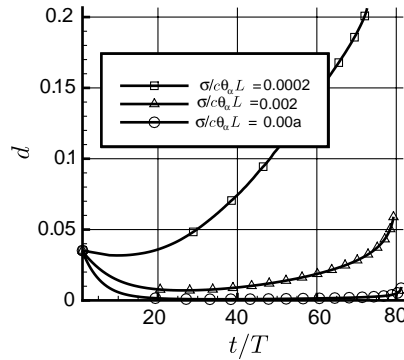

Fig. 16. Deviation d from the average radius as a function of normalized time for different values of the normalized interfacial free-energy density $\sigma/c\theta_\alpha L$.
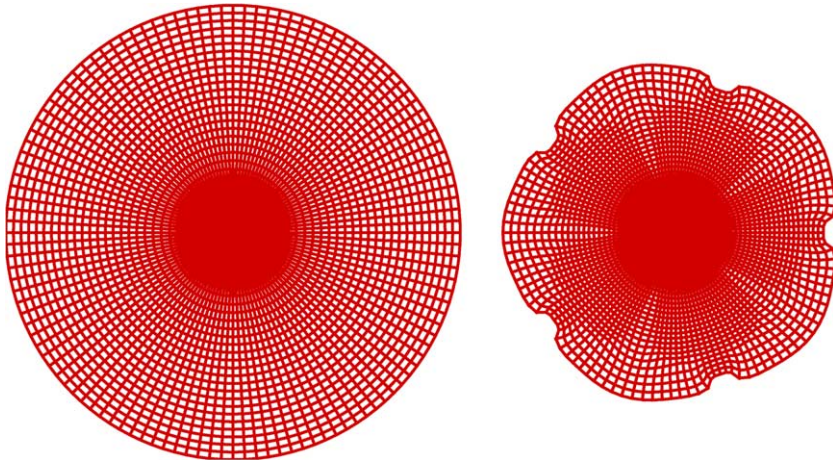

Fig. 17. Deformed meshes at (left) the initial time and (right) a final time for the perturbed interface problem with free-energy density $\sigma/c\theta_\alpha L = 0.0002$.

We define the measure

$$d = \sqrt{\frac{\int_{\mathcal{S}} (r - r_{\mathrm{avg}})^2 \, \mathrm{d}a}{\int_{\mathcal{S}} r_{\mathrm{avg}}^2 \, \mathrm{d}a}}, \tag{5.12}$$

as an indicator for the deviation from the average radius r_{avg}. Fig. 16 shows the evolution in d with normalized time for various values of σ. We observe that the perturbation in the geometry is better contained by larger interfacial free-energy densities.

Finally, we find it illustrative to compare the deformed configurations at initial and final stages of perturbed interface evolution in Fig. 17. As the collapsed phase grows at the expense of the swollen, the overall specimen dimensions decrease. Moreover, the perturbed interface geometry gives rise to a pattern that can clearly be observed on the surface of the specimen as shown in the figure.

6. Summary and concluding remarks

In this paper, we presented a sharp interface model to describe the thermally induced swelling of stimulus–responsive hydrogels. This model is built upon the work of Gurtin and Voorhees (1993) and incorporates our previous efforts for chemically induced swelling (Dolbow et al., 2004). The model considers the coupled effects of thermal transport and force balance and their influence on the motion of a sharp interface separating swollen and collapsed gel phases. We view this as an important step toward the development of a more complete theory incorporating heat and mass transport and their coupling with the stress response in SRHs.

After stating the kinematic assumptions and fundamental balance laws, we provided constitutive equations appropriate for gel-like substances. An operator split was then developed to decouple the resulting mechanical and thermal evolution equations and these equations were recast in equivalent variational forms. Enriched approximations to the motion and temperature fields were used to capture discontinuities at the phase interface without remeshing. The interface was represented as the zero-level set of some function and a simplified strategy was employed to solve the non-linear advection equation for that function. Domain integral approximations were used to evaluate the interfacial quantities including the driving traction, heat flux, and geometric descriptors of the interface. We presented results from simulations of the swelling kinetics of spherical and cylindrical gel specimens. Our model was found to be able to predict different threshold temperatures for swollen $\rightarrow$ collapsed and collapsed $\rightarrow$ swollen transitions in agreement with experimental observations.

Acknowledgments

References

Atkinson, C., Eshelby, J.D., 1968. The flow of energy into the tip of a moving crack. International Journal of Fracture 4, 3–8.
Bellec, J., Dolbow, J.E., 2003. A note on enrichment functions for crack nucleation. Communications in Numerical Methods in Engineering 19 (12), 921–932.
Belytschko, T., Black, T., 1999. Elastic crack growth in finite elements with minimal remeshing. International Journal for Numerical Methods in Engineering 45 (5), 601–620.

Carey, G.F., Chow, S.S., Seager, M.K., 1985. Approximate boundary-flux calculations. Computer Methods in Applied Mechanics and Engineering 50, 107–120.

Chadwick, P., 1974. Thermo-mechanics of rubberlike materials. Philosophical Transactions of the Royal Society of London A 276, 371–403.

Chadwick, P., Creasy, C.F.M., 1984. Modified entropic elasticity of rubberlike materials. Journal of the Mechanics and Physics of Solids 32, 337–357.

Dolbow, J., 1999. An extended finite element method with discontinuous enrichment for applied mechanics. Ph.D. Thesis, Northwestern University.

Dolbow, J.E., Devan, A., 2004. Enrichment of enhanced assumed strain approximations for representing strong discontinuities: addressing volumetric incompressibility and the discontinuous patch test. International Journal for Numerical Methods in Engineering 59 (1), 47–67.

Dolbow, J.E., Fried, E., Ji, H., 2004. Chemically-induced swelling of hydrogels. Journal of the Mechanics and Physics of Solids 52, 51–84.

Dolbow, J.E., Fried, E., Ji, H., in press. A numerical strategy for investigating the kinetics of stimulus–responsive hydrogels. Computer Methods in Applied Mechanics and Engineering.

Eshelby, J.D., 1951. The force on an elastic singularity. Philosophical Transactions of the Royal Society of London A 244, 87–112.

Eshelby, J.D., 1956. The continuum theory of lattice defects. In: Seitz, F., Turnbull, D. (Eds.), Progress in Solid State Physics 3. Academic Press, New York.

Eshelby, J.D., 1970. Energy relations and the energy-momentum tensor in continuum mechanics. In: Kanninen, M.F., Alder, W.F., Rosenfield, A.R., Jaffe, R.I. (Eds.), Inelastic Behavior of Solids. McGraw-Hill, New York.

Garikipati, K., Rao, V.S., 2001. Recent advances in models for thermal oxidation of silicon. Journal of Computational Physics 174 (1), 138–170.

Gibbs, J.W., 1878. On the equilibrium of heterogeneous substances. Transactions of the Connecticut Academy of Arts and Sciences 3, 108–248.

Gurtin, M.E., 1995. The nature of configurational forces. Archive for Rational Mechanics and Analysis 131 (1), 67–100.

Gurtin, M.E., 2000. Configurational Forces as Basic Concepts in Continuum Physics. Springer, New York.

Gurtin, M.E., Struthers, A., 1990. Evolving phase boundaries in the presence of bulk deformation. Archive for Rational Mechanics and Analysis 112, 97–160.

Gurtin, M.E., Voorhees, P.W., 1993. The continuum mechanics of coherent two-phase elastic solids with mass transport. Proceedings of the Royal Society of London Series A 440 (1909), 323–343.

Herring, C., 1951. Surface Tension as a Motivation for Sintering. McGraw-Hill, New York.

Hirokawa, Y., Tanaka, T., 1984. Volume phase-transition in a nonionic gel. Journal of Chemical Physics 81 (12), 6379–6380.

Ji, H., Chopp, D., Dolbow, J.E., 2002. A hybrid extended finite element/level set method for modeling phase transformations. International Journal for Numerical Methods in Engineering 54, 1209–1233.

Ji, H., Dolbow, J.E., 2004. On strategies for enforcing interfacial constraints and evaluating jump conditions with the extended finite element method. International Journal for Numerical Methods in Engineering 61, 2508–2535.

Matsuo, E., Tanaka, T., 1988. Kinetics of discontinuous volume-phase transition of gels. Journal of Chemical Physics 89 (3), 1695–1703.

Melenk, J.M., Babuška, I., 1996. The partition of unity finite element method: basic theory and applications. Computer Methods in Applied Mechanics and Engineering 139, 289–314.

Moës, N., Cloirec, M., Cartraud, P., Remacle, J.F., 2003. A computational approach to handle complex microstructure geometries. Computer Methods in Applied Mechanics and Engineering 192, 3163–3177.

Moës, N., Dolbow, J., Belytschko, T., 1999. A finite element method for crack growth without remeshing. International Journal for Numerical Methods in Engineering 46, 131–150.

Moran, B., Shih, C.F., 1987. Crack tip and associated domain integrals from momentum and energy balance. Engineering Fracture Mechanics 127, 615–642.

Mourad, H.M., Garikipati, K., in press. Advances in the numerical treatment of grain-boundary migration: coupling with mass transport and mechanics, Journal of Computational Physics.

Mullins, W., Sekerka, R., 1963. Morphological stability of a particle growing by diffusion and heat flow. Journal of Applied Physics 34, 323–329.

Olsen, M., Bauer, J.M., Beebe, D., 2000. Particle imaging techniques for measuring the deformation rate of hydrogel microstructures. Applied Physics Letters 76 (22), 3310–3312.

Osher, S., Sethian, J., 1988. Fronts propagating with curvature dependent speed: algorithms based on Hamilton–Jacobi formulation. Journal of Computational Physics 79, 12–49.

Peach, M.O., Koehler, J.S., 1950. The forces exerted on dislocations and the stress fields produced by them. Physical Review 80, 436–439.

Rice, J.R., 1968. Mathematical analysis in the mechanics of fracture. In: Liebowitz, H. (Ed.), Fracture II, New York.

Sethian, J., 1999. Level Set Methods and Fast Marching Methods. Cambridge University Press, New York, NY.

Shibayama, M., Fujikawa, Y., Nomura, S., 1996. Dynamic light scattering study of poly(*n*-isopropylacrylamide-co-acrylic) gels. Macromolecules 29, 6535–6541.

Sukumar, N., Chopp, D.L., Moës, N., Belytschko, T., 2001. Modeling holes and inclusions by level sets in the extended finite element method. Computer Methods in Applied Mechanics and Engineering 190, 6183–6200.

Sukumar, N., Srolovitz, D.J., Baker, T.J., Prevost, J.H., 2003. Brittle fracture in polycrystalline microstructures with the extended finite element method. International Journal for Numerical Methods in Engineering 56 (14), 2015–2037.

Tanaka, T., Fillmore, D.J., 1979. Kinetics of swelling of gels. Journal of Chemical Physics 70 (3), 1214–1218.